Assimilation of Radiocarbon and Chlorofluorocarbon Data to Constrain Deep and Bottom Water Transports in the World Ocean

REINER SCHLITZER

Alfred Wegener Institute for Polar and Marine Research, Bremerhaven, Germany

(Manuscript received 11 July 2005, in final form 24 May 2006)

ABSTRACT

A coarse-resolution global model with time-invariant circulation is fitted to hydrographic and tracer data by means of the adjoint method. Radiocarbon and chlorofluorocarbon (CFC-11 and CFC-12) data are included to constrain deep and bottom water transport rates and spreading pathways as well as the strength of the global overturning circulation. It is shown that realistic global ocean distributions of hydrographic parameters and tracers can be obtained simultaneously. The model correctly reproduces the deep ocean radiocarbon field and the concentrations gradients between different basins. The spreading of CFC plumes in the deep and bottom waters is simulated in a realistic way, and the spatial extent as well as the temporal evolution of these plumes agrees well with observations. Radiocarbon and CFC observations place upper bounds on the northward transports of Antarctic Bottom Water (AABW) into the Pacific, Atlantic, and Indian Oceans. Long-term mean AABW transports larger than 5 Sv (Sv $\equiv 10^6$ m^3 s^{-1}) through the Vema and Hunter Channels in the South Atlantic and net AABW transports across 30°S into the Indian Ocean larger than 10 Sv are found to be incompatible with CFC data. The rates of equatorward deep and bottom water transports from the North Atlantic and Southern Ocean are of similar magnitude (15.7 Sv at 50°N and 17.9 Sv at 50°S). Deep and bottom water formation in the Southern Ocean occurs at multiple sites around the Antarctic continent and is not confined to the Weddell Sea. A CFC forecast based on the assumption of unchanged abyssal transports shows that by 2030 the entire deep west Atlantic exhibits CFC-11 concentrations larger than 0.1 pmol kg^{-1}, while most of the deep Indian and Pacific Oceans remain CFC free. By 2020 the predicted CFC concentrations in the deep western boundary current (DWBC) in the North Atlantic exceed surface water concentrations and the vertical CFC gradients start to reverse.

1. Introduction

The formation of dense waters at high latitudes and the subsequent sinking and spreading of the water in the abyssal ocean are integral parts of the global ocean's overturning circulation. This overturning circulation has profound effects on the heat budget of the earth and impacts the regional and global climate. Apart from heat, the sinking waters also carry dissolved constituents, such as oxygen, nutrients, and CO_2, and the strength of the overturning circulation ultimately determines the oxygen, nutrient, and carbon levels in the abyss. Deep-water nutrients in turn affect ocean productivity in regions where the waters are brought back to the surface. Sinking and spreading of dense water masses also contributes to the uptake and sequestration of anthropogenic CO_2 by the ocean (Orr et al. 2001) and affects atmospheric CO_2 concentrations. Quantitative assessment of the respective property budgets requires the knowledge of water mass formation rates and transports in the global ocean.

However, while the ocean circulation near the surface is relatively well understood, our knowledge about the patterns and strengths of the abyssal circulation is still limited, and uncertainties of formation rates and transports are still large. This is due to the costs and logistical difficulties of direct observations in the deep sea but is also due to the complexity of the formation processes Marshall and Schott (1999). Except for a few regions in the World Ocean, where direct flow measurements have been made over longer time periods, most of our knowledge about deep ocean circulation on large scales comes from inferences made on the basis of distributions of hydrographic parameters, such as temperature, salinity, oxygen, nutrients, and other tracers

Corresponding author address: Reiner Schlitzer, Alfred Wegener Institute, Columbusstrasse, D-27568 Bremerhaven, Germany. E-mail: rschlitzer@awi-bremerhaven.de

DOI: 10.1175/JPO3011.1

(Mantyla and Reid 1995; Reid 1997; Wunsch and Grant 1982; Wunsch et al. 1983).

Using measurements of the radioactive carbon isotope ^{14}C, Broecker and Peng (1982) were able to determine the ages of deep water masses (time since last surface contact) and could establish overturning time scales and water mass renewal times for individual basins and the global ocean. Other tracers, such as tritium, ^{3}He, and ^{39}Ar, have also been used to estimate deep water formation and transport rates. However, the substances most extensively sampled and used since the 1980s are the chlorofluorocarbons (CFCs). CFCs are man-made gases that are released into the atmosphere in growing amounts since about 1940. They dissolve in surface waters and are carried into the abyssal ocean with the newly formed dense water masses. Tongues of enhanced CFC concentrations form along deep and bottom water spreading paths (Weiss et al. 1985), and the observed CFC distributions can be used to estimate spreading velocities and transport rates (Andrie et al. 2002; Bullister and Weiss 1983; Meredith et al. 2001: Orsi et al. 2002; Rhein et al. 2002; Smethie and Fine 2001).

Large global datasets consisting of observations from the World Ocean Circulation Experiment (WOCE) and numerous non-WOCE cruises are now available for the suite of carbon parameters, including radiocarbon (Key et al. 2004), and for the CFCs (WOCE Data Products Committee 2002). These global datasets are widely used for a variety of scientific problems, including the estimation of water mass ages (Fine et al. 2002) and the quantification of biogeochemical processes, such as oxygen utilization (Feely et al. 2004) or CO_2 uptake (Matear et al. 2003). In recent years, CFCs are also used increasingly for model validation (Böning et al. 2003; Dutay et al. 2002; England and Maier-Reimer 2001; Matsumoto et al. 2004).

Here, a new model is presented that exploits the available large datasets for the tracers and automatically varies the model's flow field until optimal agreement with the data is reached. Unlike in other model studies where CFCs and radiocarbon are only used to assess a given model state, here the tracer data actively influence and determine the final optimal solution. The adjoint formalism used for the fitting procedure is described in section 2. The optimal tracer fields of the model and the deep and bottom water flows required for realistic ^{14}C and CFC simulations are presented and discussed in section 3. Section 4 contains a summary of the main results of the study.

2. Model and data

The model used in this study is an extension of the adjoint model of de las Heras and Schlitzer (1999) and Schlitzer (2000) that has previously been fitted to global hydrographic, nutrient, oxygen, and carbon fields. The general model strategy is described in detail in Schlitzer (1993, 1995, 2000). Model applications aimed at the estimation of marine export production and biogeochemical fluxes can be found in Schlitzer (2002, 2004) and Schlitzer et al. (2004). In the following, the general model setup is described briefly. Emphasis is on the extensions with respect to the assimilation of natural radiocarbon and CFC data. The notation follows that in Schlitzer (2000).

The model is of global extent and uses a nonuniform grid with horizontal resolution ranging between $1° \times 1°$ and $4° \times 5°$ latitude $\times$ longitude. High resolution is implemented in regions with narrow currents (Drake Passage, Atlantic Ocean part of the Antarctic Circumpolar Current, the Indonesian and Caribbean archipelagos), along coastal boundaries with strong currents (Florida Current, Gulf Stream, Brazil Current, Agulhas Current, Kuroshio), over steep topography (Greenland–Iceland–Scotland overflow region), and in areas with pronounced coastal upwelling or downwelling. In all cases the refinements are implemented in the direction of the strongest property gradients (usually perpendicular to fronts and currents) to better trace changes in ocean properties.

The model has 26 vertical layers, with thickness progressively increasing from 60 m at the surface to approximately 500 m at 5000-m depth. Realistic topography is used, based on the U.S. Navy bathymetric data and averaged over grid cells. Model depths over ridges and in narrow channels are adjusted manually to respective sill or channel depths. The model has three open boundaries, along which ocean properties and transports are prescribed in each model layer. They are located at the exit of the Mediterranean Sea, Red Sea, and Persian Gulf. These three marginal seas are not modeled explicitly, but their impact on the global circulation is taken into account.

a. Independent parameters

The overall goal of the model calculations is to find optimal values for a set of physical and biogeochemical parameters defined on the model grid:

$$\mathbf{p}^* = [u_i, \upsilon_i, K_h, K_\upsilon, Q_i, \mathrm{EP}_i, \beta_i]^{\mathrm{T}}. \quad (1)$$

Included in the vector of *independent* parameters $\mathbf{p}^*$ are zonal and meridional oceanic flows (u, υ), isopycnal and diapycnal mixing coefficients (K_h, K_υ), air–sea fluxes of heat and gases (Q), and biological production rates in the ocean surface layer (export production EP), as well as downward fluxes and remineralization rates of par-

ticulate matter (β). For reasons of computational efficiency and because of the sparseness of the available hydrographic and tracer datasets, which provide seasonal or interannual resolution at only a few time series stations worldwide, all physical and biogeochemical transports and rate constants in the model are considered to be time invariant, and temporal variability in these fields is neglected. The model results therefore represent climatological mean fields, which are valid for the time periods spanned by the datasets assimilated by the model (ca. 1950–2000).

The parameters in $\mathbf{p}^*$ can be varied and adjusted independently by the model, and the ultimate objective is to find optimal values for the elements in $\mathbf{p}^*$. To be considered optimal, the parameters have to satisfy as closely as possible a number of formalized criteria that are all represented as real-valued penalty terms in the model's cost function F. The most important cost function terms of the present model are constraints on the vertical velocity shear, linked to geostrophic shear estimates obtained from hydrographic data, and the requirement that the simulated distributions of temperature, salinity, nutrients, oxygen, carbon, radiocarbon, and CFC (hereinafter collectively called tracers) match the observations accurately. The velocity shear constraints in the cost function are the model's way of implementing the geostrophic principle: the shape of the velocity profiles are required to be close to geostrophic profiles while constant offsets are allowed without penalty. Unlike in other inverse models, which enforce exact matches with estimated geostrophic shears, here, the model shears may deviate from geostrophic estimates within the uncertainties of the estimates. Details on additional dynamical constraints and smoothness terms in F can be found in Schlitzer (1993). The problem of finding optimal values for $\mathbf{p}^*$ is equivalent to finding a minimum of F.

b. Tracer budgets

Model tracer values are defined at the centers of the grid boxes whereas flows are defined on the interfaces (Arakawa C grid). Mass and tracer budget equations are formulated for every model box, and for all tracers except CFC, long-term mean, steady-state tracer distributions are calculated as solutions of the steady-state budget equations formulated for the boxes of the model:

$$\sum_i A_i(u_i c_i - K_h \nabla c_i) + \sum_j A_j(v_j c_j - K_h \nabla c_j) + \sum_k A_k(w_k c_k - K_v \nabla c_k) - q = 0. \quad (2)$$

In (2) summation is over all interfaces of a box, A is the area of an interface and has either a positive or negative sign depending on whether a positive flow u, v, or w (eastward, northward, or upward) enters or leaves the box; c and ∇c are tracer concentration and surface-normal tracer gradients on the respective interfaces; and q includes air–sea fluxes and internal source or sink terms, such as radioactive decay, biogeochemical production, or particle remineralization. A weighted averaging scheme is used to express the interface concentrations c in terms of the upwind and downwind box concentrations c_u and c_d:

$$c = f_u c_u + (1 - f_u) c_d. \quad (3)$$

Here, $f_u = 0.7$ is chosen, resulting in a hybrid tracer advection scheme that combines the numerical stability of the upwind scheme ($f_u = 1$) with the low numerical diffusion of the centered scheme ($f_u = ½$).

Setting $c = 1$, $\nabla c = 0$, and $q = 0$ in (2) yields the mass conservation equations, which are used to calculate the vertical model flows w, based on the zonal and meridional flows u and v. The w calculation is done column-wise, starting with the bottom-most box and assigning any net in- or outflow arising from the fluxes from the sides and from below to the transport across the top interface of a box.

Formulation of the budget Eq. (2) for a given tracer for all n_b boxes of the model results in a set of n_b coupled linear equations for the unknown box tracer concentrations c, which can be expressed in matrix–vector notation as

$$\mathbf{T} \cdot \mathbf{c} = \mathbf{q}, \quad (4)$$

where $\mathbf{T}$ is the square advection–diffusion transport matrix and $\mathbf{c}$ is the vector of the tracer concentrations for all n_b boxes. The vector on the right-hand-side $\mathbf{q}$ contains the source–sink terms and boundary fluxes for each of the n_b boxes. The transport matrix $\mathbf{T}$ depends on the circulation and mixing of the model, and is the same for all tracers, except for radiocarbon and CFC (see below). For the other tracers, the budget equations only differ in the boundary fluxes and source–sink terms contained in the right-hand-side $\mathbf{q}$. Calculation of the different unknown tracer concentrations $\mathbf{c}$ therefore requires solving many systems of linear equations, which all have the same coefficient matrix $\mathbf{T}$ and only differ in the right-hand-side $\mathbf{q}$. Solutions are most efficiently obtained by applying a sparse $\mathbf{LU}$ factorization algorithm (Harwell 1995) on $\mathbf{T}$, and then using the factorization and the different right-hand sides for computationally cheap solution steps. The availability of the $\mathbf{LU}$ factor matrices also allows efficient solving of the associated adjoint equations involving the transpose

of the transport matrix $\mathbf{T}^{\mathrm{T}}$ (see below). Surface boundary conditions for all tracers except radiocarbon and CFC are formulated as flux boundary conditions, and the respective air–sea tracer fluxes (if applicable) are contained in $\mathbf{q}$.

c. Radiocarbon

For radiocarbon (and CFC; see below) surface concentration boundary conditions are used instead of flux conditions, because ^{14}C and CFC concentrations are better known than fluxes. Consequently, the distributions of these two tracers are simulated only for model layers 2 and deeper (for a total of n_i interior boxes), while the values in layer 1 are specified. This leads to smaller tracer budget systems [Eq. (4)] as compared with the other hydrographic parameters. Another difference for radiocarbon is the contribution of the decay term with the diagonal elements of the radiocarbon transport matrix $\mathbf{T}$. Internally, radiocarbon concentrations are represented as relative ^{14}C/^{12}C abundance ratios:

$$c_C = 1 + \Delta^{14}\mathrm{C}/1000, \tag{5}$$

where Δ^{14}C is the ^{14}C value in the usual Δ notation. The advantage of using ^{14}C/^{12}C ratios instead of absolute ^{14}C concentrations is that biological effects can be largely ignored (Fiadeiro 1982), as they affect ^{14}C and ^{12}C in the same manner. The radiocarbon surface boundary concentrations are taken from Key et al. (2004), who provide estimates of natural ^{14}C for the World Ocean. Natural Δ^{14}C values in low- and midlatitude surface waters are typically between −45‰ and −65‰, while much lower values between −100‰ and −120‰ are found in the Southern Ocean. Solutions for the unknown model ^{14}C values in the ocean interior are obtained by first calculating the $\mathbf{LU}$ factorization of the radiocarbon coefficient matrix and then using the factorization in the solution step. As for the other tracers, the factorization matrices are reused in solving the associated adjoint model (see below).

d. CFCs

CFC-11 and CFC-12 are the only time-dependent tracers in the present model. Their temporal evolution in the ocean interior is simulated by applying time-varying CFC surface boundary concentrations and an implicit forward time-stepping scheme. Analysis of observed CFC saturation levels shows that low- and midlatitude surface waters generally are in close equilibrium with the overlying atmosphere. In polar and subpolar waters, however, seasonal or permanent ice cover as well as vigorous vertical water mass exchange typically prevent surface waters from reaching full equilibrium, and saturation levels can be as low as 60%–80% (Orsi et al. 2002; Smethie and Jacobs 2005). Regional CFC saturation levels estimated from CFC observations are taken into account for the construction of the time-varying CFC surface boundary values of the model. It is assumed that in the surface water the degree of saturation remains constant in time, and time-dependent surface boundary values are then obtained by applying the observed atmospheric CFC trends (Walker et al. 2000).

Model CFC distributions are calculated for the period between 1950 and 2004 using an implicit time-stepping procedure and zero initial CFC concentrations at the start of the integration. Once the CFC concentrations $\mathbf{c}_k$ are known for a given time t_k, the concentrations $\mathbf{c}_{k+1}$ at the next time $\mathrm{t}_{k+1} = t_k + \Delta t$ are obtained as follows:

$$(\mathbf{c}_{k+1} - \mathbf{c}_k)/\Delta t = \mathbf{T} \cdot \mathbf{c} + \mathbf{b}. \tag{6}$$

In (6), $\mathbf{T}$ is the advection–diffusion transport matrix for CFCs, $\mathbf{c} = (\mathbf{c}_{k+1} + \mathbf{c}_k)/2$ are the CFC concentrations evaluated at the middle of the time interval $t = (t_{k+1} + t_k)/2$ that are actually transported by $\mathbf{T}$, and $\mathbf{b}$ is the vector of CFC fluxes from the boundaries, also evaluated at midtime t. Substituting $\mathbf{c}$ and reordering the terms yields a matrix equation for the unknown concentrations $\mathbf{c}_{k+1}$ at the new time:

$$(\mathbf{I} - \tilde{\mathbf{T}}) \cdot \mathbf{c}_{k+1} = (\mathbf{I} + \tilde{\mathbf{T}}) \cdot \mathbf{c}_k + \tilde{\mathbf{b}}, \tag{7}$$

where $\tilde{\mathbf{T}}$ and $\tilde{\mathbf{b}}$ are the transport matrix $\mathbf{T}$ and boundary flux vector $\mathbf{b}$ scaled with $\Delta t/2$ and Δt, respectively, and $\mathbf{I}$ is the identity matrix. Finding the CFC concentrations for a new time step using an implicit numerical scheme thus involves solving a system of linear equations and in terms of algorithms and computational cost is equivalent to the task of calculating the steady-state distributions for any of the other tracers in the model.

It is important to note that the coefficient matrix of the system $(\mathbf{I} - \tilde{\mathbf{T}})$ remains the same for all time steps, and only the right-hand sides change from step to step. Again, a solver based on $\mathbf{LU}$ factorization of the matrix is most efficient, since the factorization step has to be performed only once, while the factor matrices can be used for all time steps in the relatively cheap solving phases. As an additional benefit, the $\mathbf{LU}$ factor matrices are also used to solve the associated CFC adjoint equations (see below).

The great advantage of implicit-in-time numerical schemes is their stability and the accommodation of relatively large time steps. In the present case the model was operated with a 2-yr step, which required only 27 time-step calculations and allowed for the re-

tention of the full model CFC histories in the computer's memory. This is essential for an efficient solving of the CFC adjoint as will be seen below. Sensitivity runs with a much smaller 0.2-yr time step showed negligible CFC concentration differences of less than 1‰. The 2-yr time step is much larger than the air–sea equilibration times for CFC; however, this does not imply CFC equilibrium at the sea surface since we apply realistic surface concentration boundary conditions (see above).

e. Dependent parameters

The vertical velocities w and the simulated distributions c of all tracers in the model (CFC fields for all time steps; steady-state fields for the other tracers) compose the set of dependent parameters of the model:

$$\tilde{\mathbf{p}} = [w_i, c_i]^{\mathrm{T}}. \tag{8}$$

Given values for the independent model parameters $\mathbf{p}^*$, all the dependent parameters $\tilde{\mathbf{p}}$ can be calculated by applying the mass and tracer budget equations described above. Note that there is one dependent parameter for every budget equation considered. For mass and the steady-state tracers there are n_b budget equations each, for radiocarbon there are n_i equations, and for the CFCs there are n_i budget equations for every time step (n_i is the number of interior boxes). All tracer budget equations can be reordered and written in the following homogenous form:

$$E_i = 0, \quad i = 1, \ldots, n_e. \tag{9}$$

This form will be used in the adjoint formulation below.

f. Cost function

Once calculated, the simulated tracer concentrations c_i in the model are compared with values derived from measurements d_i, and misfit terms normalized by the errors of the data values σ_i are accumulated in the cost function F of the model:

$$F(\mathbf{p}^*, \tilde{\mathbf{p}}) = \cdots + \left(\frac{c_i - d_i}{\sigma_i}\right)^2 + \cdots, \tag{10}$$

where the d_i are box averages calculated from the historical hydrographic and tracer datasets. For the steady-state tracers the box averages include all available data from all years, months, or seasons, whereas for the time-varying CFCs, box averages are calculated for 3-month periods. Comparisons are performed for those boxes (and time steps in the case of CFC) that contain data. Radiocarbon data for boxes with significant CFC concentrations, either in the upper ocean or in recently ventilated deeper water masses are believed to be contaminated with atomic bomb radiocarbon and are excluded from the ^{14}C comparison. In addition to the misfit terms in (10), the cost function F contains many other terms, some of which also involve the independent parameters $\mathbf{p}^*$. For details see Schlitzer (1993, 1995, 2000, 2002, 2004).

When searching for the minimum of the cost function F, only the independent parameters $\mathbf{p}^*$ may be varied freely, while the dependent parameters $\tilde{\mathbf{p}}$ are uniquely determined by the n_e model budget equations $E_i = 0$. The problem of finding the smallest value of F therefore is a constrained minimization problem, which can be efficiently solved with the method of Lagrange multipliers, also denoted in meteorology and oceanography as the *adjoint* method (Le Dimet and Talagrand 1986; Schlitzer 2000; Thacker and Long 1988).

g. Adjoint equations

With the n_e model equations $E_i = 0$ and the cost function F, the Lagrangian L of the problem is given by

$$L(\mathbf{p}^*, \tilde{\mathbf{p}}, \lambda) = F(\mathbf{p}^*, \tilde{\mathbf{p}}) + \sum_{j=1}^{n_e} \lambda_j \cdot E_j, \tag{11}$$

where λ_j are n_e yet unknown Lagrange multipliers. Note that L is a function of model parameters $\mathbf{p}^*$ and $\tilde{\mathbf{p}}$ as well as of the Lagrange multipliers $\boldsymbol{\lambda}$. In optimization theory it is shown by, for example, Hestenes (1975) that the minimum of F is a stationary point of L, at which all partial derivatives of L with respect to the Lagrange multipliers $\boldsymbol{\lambda}$ as well as the dependent and independent parameters $\tilde{\mathbf{p}}$ and $\mathbf{p}^*$ vanish:

$$\frac{\partial L}{\partial \lambda_j} = E_j = 0, \tag{12}$$

$$\frac{\partial L}{\partial \tilde{p}_i} = \frac{\partial F}{\partial \tilde{p}_i} + \sum_{j=1}^{n_e} \lambda_j \cdot \frac{\partial E_j}{\partial \tilde{p}_i} = 0 \quad \text{and} \tag{13}$$

$$\frac{\partial L}{\partial p_i^*} = \frac{\partial F}{\partial p_i^*} + \sum_{j=1}^{n_e} \lambda_j \cdot \frac{\partial E_j}{\partial p_i^*} = 0. \tag{14}$$

The derivatives in (11), (12), and (13) are calculated as though the λ_i, $\tilde{p}_i$, and p_i^* were independent. Differentiation with respect to the Lagrange multipliers (12) recovers the model Eqs. (9), and differentiation with respect to the dependent and independent model parameters $\tilde{\mathbf{p}}$ and $\mathbf{p}^*$ yields the adjoint in Eqs. (13) and (14). Seeking the minimum of F is equivalent to finding a model solution that satisfies (12), (13), and (14). The Lagrange multipliers λ_j are calculated by solving (13) with $\partial L/\partial \tilde{p}_i$ set to zero. Introducing the λ_j into (14) then yields the gradient of F given by $\nabla F = \partial L/\partial p_i^*$. This gradient is then passed to a descent algorithm (here a limited-memory, quasi-Newton conjugate gradient al-

gorithm) to obtain a new, improved model state $\mathbf{p}^*_{\text{new}}$ with a smaller value of the cost function F.

h. Adjoint implementation

The dimension n_e of the homogenous linear system (13),

$$\sum_{j=1}^{n_e} \frac{\partial E_j}{\partial \tilde{p}_i} \lambda_j = -\frac{\partial F}{\partial \tilde{p}_i}, \tag{15}$$

used to calculate the unknown Lagrange multipliers λ_j tends to be very large. For the present, relatively coarse resolution model there are more than 3.2 million equations, most of which arise from the CFC-11 and CFC-12 time-stepping equations in (7). It is important to note that this huge system can be separated into much smaller linear systems, one for each tracer in the model, and that the Lagrange multipliers associated with the different tracers can be calculated separately. This follows from the fact that the budget equations $E_j = 0$ of a given tracer do not contain the concentration values (dependent parameters $\tilde{p}_i$) of the other tracers, and the respective derivatives $\partial E_j/\partial \tilde{p}_i$ therefore vanish.

For a tracer with model equations $\mathbf{T} \cdot \mathbf{c} - \mathbf{q} = 0$ [see (4) above] the partial derivative of the jth equation E_j with respect to the ith concentration $\tilde{p}_i = c_i$ evaluates to $\partial E_j/\partial \tilde{p}_i = T_{ji}$, and (15) can be rewritten as

$$\mathbf{T}^{\mathrm{T}} \cdot \boldsymbol{\lambda} = -\frac{\partial F}{\partial \tilde{p}_i}. \tag{16}$$

Thus, the Lagrange multipliers for a given tracer are the solution of a linear system closely related to the model equations of that tracer, and the transpose of the coefficient matrix in the model equations serves as a coefficient matrix of the Lagrange multiplier equations.

For the time-dependent CFCs the situation is somewhat more complicated. The concentration values $\mathbf{c}_k$ (dependent parameters $\tilde{p}_i$) for any given time step k, except the very last one n, occur in the budget equations of two steps—first in step k, during which $\mathbf{c}_k$ is calculated, and second in the following step $k + 1$:

$$k: \quad (\mathbf{I} - \tilde{\mathbf{T}}) \cdot \mathbf{c}_k - (\mathbf{I} + \tilde{\mathbf{T}}) \cdot \mathbf{c}_{k-1} - \tilde{\mathbf{b}}_k = 0 \quad \text{and} \tag{17}$$

$$k + 1: \quad (\mathbf{I} - \tilde{\mathbf{T}}) \cdot \mathbf{c}_{k+1} - (\mathbf{I} + \tilde{\mathbf{T}}) \cdot \mathbf{c}_k - \tilde{\mathbf{b}}_{k+1} = 0. \tag{18}$$

Nonzero partial derivatives of model equations with respect to $\mathbf{c}_k$ therefore occur for both steps and evaluate to $\partial(E_k)_j/\partial(c_k)_i = (\mathbf{I} - \tilde{\mathbf{T}})_{ji}$ (step k) and $\partial(E_{k+1})_j/\partial(c_k)_i = -(\mathbf{I} + \tilde{\mathbf{T}})_{ji}$ (step $k + 1$). Summation in (13) over all model equations and reordering of terms yields

$$(\mathbf{I} - \tilde{\mathbf{T}})^{\mathrm{T}} \cdot \boldsymbol{\lambda}_k = (\mathbf{I} + \tilde{\mathbf{T}})^{\mathrm{T}} \cdot \boldsymbol{\lambda}_{k+1} - \nabla_{\mathbf{c}_k} F, \quad k = 1, \ldots, n - 1. \tag{19}$$

For the last time step $k = n$, there is no contribution from a subsequent step $k + 1$, and one obtains

$$(\mathbf{I} - \tilde{\mathbf{T}})^{\mathrm{T}} \cdot \boldsymbol{\lambda}_n = -\nabla_{\mathbf{c}_n} F. \tag{20}$$

Taken together, (20) and (19) provide a backward-stepping algorithm for the sequential calculation of all Lagrange multipliers associated with the CFC budget equations: one starts with (20) and solves for the Lagrange multipliers for the last time step $\boldsymbol{\lambda}_n$, then $\boldsymbol{\lambda}_n$ is substituted into (19) and $\boldsymbol{\lambda}_{n-1}$ is calculated. This procedure is repeated until the Lagrange multipliers for all time steps are calculated. For each step k of the backward calculation of Lagrange multipliers ($k = n, \ldots, 1$), the CFC model–data differences have to be evaluated for the given time interval k, and the gradient of F with respect to the CFC concentrations $\mathbf{c}_k$ has to be calculated and substituted into the right-hand sides of (20) and (19). Therefore, the full time history of simulated CFC concentrations has to be accessible during backward Lagrange multiplier calculation. In the present model, the long time step of the implicit scheme and the small number of required time steps allows us to keep the full CFC model histories in the computer's memory, thereby avoiding inefficient and time-consuming saving and retrieving to and from disk files.

Note that the calculation of the Lagrange multipliers in both the steady-state and time-dependent cases involves solving linear systems of equations that are very closely related to the original model equation systems. The coefficient matrices are given as a transpose of the original matrices, and the right-hand sides consist of the gradients of the cost function F with respect to the simulated tracer concentrations. Model tracer misfits as described in (10) contribute to the right-hand sides and therefore influence the magnitudes of the Lagrange multipliers, which in turn affect the gradients of the cost function F with respect to the independent parameters $\mathbf{p}^*$ (14). Using a solver based on the **LU** factorization for the tracer simulations offers the advantage of calculating the Lagrange multipliers at very little additional computational cost, as the **LU** factor matrices can also be used for the solution of the transposed system.

Overall, the model calculations proceed according to the following steps:

1) initialize the independent parameters $\mathbf{p}^*$;
2) calculate the dependent parameters $\tilde{\mathbf{p}}$ using steady-state and time-dependent tracer budget equations;
3) calculate the value of the cost function F;

4) calculate the gradient of F $\nabla F = \partial L/\partial p^*$, by solving the adjoint equations in (13) and (14);
5) use ∇F in a descent algorithm to obtain a new, improved set of independent model parameters $\mathbf{p}^*_{\text{new}}$; and
6) return to step 2 unless a stopping criteria (i.e., indicating that the minimum has been reached) is met.

Step 2 is usually referred to as running the *forward model*. Its most computationally intensive part is the calculation of the model tracer fields, which involves solving large (but sparse) sets of linear equations. The calculation of the w is comparatively cheap. For each run of the forward model, one run of the adjoint model (step 4) is needed to complete one iteration. The availability of the **LU** factorization from the forward run allows for the efficient solving of the adjoint equations with little additional computational cost.

In the present model the number of boxes and the dimensions of the linear systems to be solved are on the order of 45 000. Because any given box is connected to only a very small number of neighboring boxes, the number of terms in any of the budget equations is quite small and the coefficient matrices are sparse. The sparse **LU** factorization method applied in the present case proved to be very efficient, and, in contrast to iterative solvers, has the advantage of providing exact solutions. Completing a single full model cycle consisting of forward simulations as well as cost function calculation and adjoint runs for ten steady-state tracers (potential temperature, salinity, oxygen, phosphate, nitrate, silicate, dissolved inorganic carbon, alkalinity, dissolved organic carbon, and natural radiocarbon) and two 60-yr-long simulations for CFC-11 and CFC-12 only takes about 40 s on a high-end personal computer. Being able to do single forward and adjoint runs quickly is an indispensable prerequisite for full model optimizations, which require thousands of these cycles.

i. Data

The present model assimilates a large number of classical hydrographic parameters and tracers (temperature, salinity, oxygen, phosphate, nitrate, silicate, dissolved inorganic carbon, alkalinity, radiocarbon, CFC-11, and CFC-12) and exploits existing large global data compilations for these variables. The recent Global Ocean Data Analysis Project (GLODAP) dataset of Key et al. (2004) is used for radiocarbon. This collection contains more than 20 000 ^{14}C data points for almost 1200 stations from WOCE and pre-WOCE cruises (Fig. 1). The data coverage is good and all major water masses in the World Ocean are represented. The typical accuracy of individual Δ^{14}C data values is between 2‰ and 5‰.

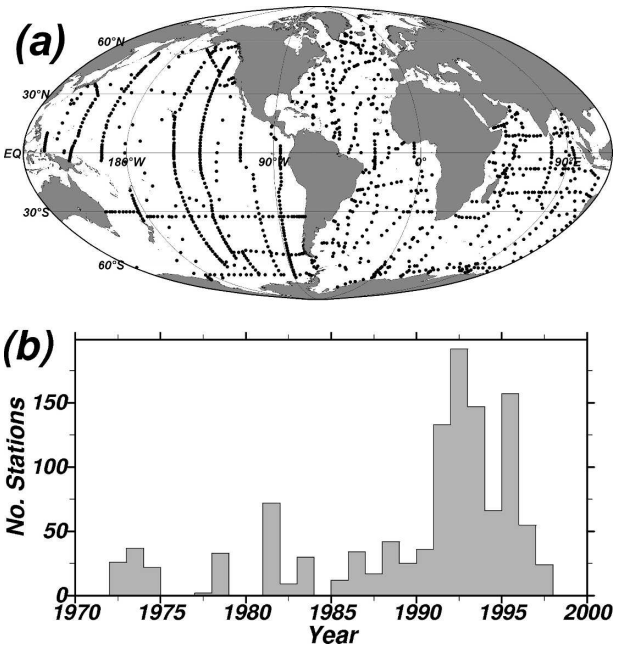

FIG. 1. (a) Map and (b) temporal distribution of ^{14}C stations from the GLODAP dataset (Key et al. 2004) used in the present study. The total number of stations is 1171, most of which are from the WOCE period 1990–2000. The collection contains 20 191 individual Δ^{14}C measurements.

For the CFCs a separate data compilation is used, mainly consisting of WOCE measurements, but complemented with numerous pre-WOCE and two recent, post-WOCE cruises (Fig. 2). Overall, the CFC dataset covers the period from 1982 to 2003 and consists of more than 150 000 CFC-11 and CFC-12 measurements at more than 8000 stations. The spatial data coverage for the combined dataset is good; however, for shorter time periods or single years the respective CFC observations are sparse and distributed heterogeneously. Only very few areas such as the deep western boundary current (DWBC) region in the northwest and tropical Atlantic have repeated CFC observations over longer time periods. The estimated accuracy of individual CFC data values is 1% or 0.02 pmol kg^{-1}, whichever is larger.

3. Results and discussion

The present study builds on a previous optimization with the same model (experiment A), which assimilated the full suite of tracers listed above, except natural radiocarbon and CFC. This model solution reproduces the classical hydrographic parameters, oxygen, and dis-

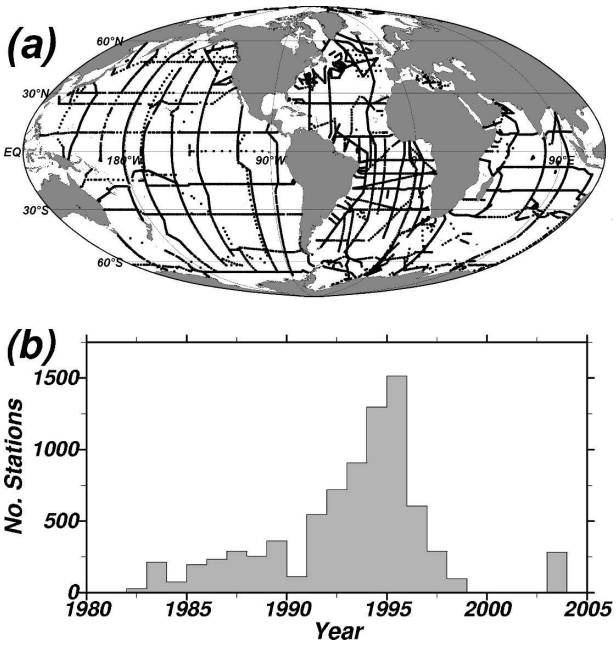

FIG. 2. (a) Map and (b) temporal distribution of CFC-11 stations used in the present study. The dataset consists mainly of WOCE data, but also includes pre-WOCE cruises reaching back to 1982. Three Atlantic cruises from the U.S. Repeat Hydrography program are also included. The collection contains 8026 stations and 154 690 individual CFC-11 measurements.

solved nutrients realistically. However, forward simulations of ^{14}C and CFC conducted as part of the Ocean Carbon Modeling Intercomparison Project (OCMIP) showed that the Southern Ocean is ventilated too rapidly and that simulated deep radiocarbon and CFC concentrations are much higher than observed (Dutay et al. 2002). In the Southern Ocean bottom waters, for instance, the simulated CFC-11 concentrations for 1998 exceed the observed values by about 0.8 pmol kg^{-1}, that is, by more than 190% of the measured values (Table 1). Bottom waters in the South Pacific Ocean (factor 150!), Indian Ocean (+600%), and South Atlantic (+110%) are also significantly higher than observations, whereas in the North Atlantic the modeled CFC-11 concentrations in the upper and lower branches of the DWBC agree within 30% when compared with the data. The radiocarbon values of experiment A are also much higher than for the measurements, again indicating too rapid vertical overturning and abyssal flows in solution A. Simulated bottom water radiocarbon concentrations are about 47‰ higher than the observations on the global average, and the largest ^{14}C deviations are found in the North Pacific, where the model exceeds the data by +66‰.

Solution A was used as the initial model state for the full tracer optimizations including radiocarbon and CFC (experiment B). About 16 000 iterations consisting of forward tracer simulations and associated solutions of the adjoint Eqs. (13) and (14) were required until the stopping criterion was met and the decrease of the cost function F per iteration was below the specified threshold. In the following chapters, the resulting optimal model radiocarbon and CFC-11 distributions are presented. It is shown that realistic fields can be obtained for all classical hydrographic parameters as well as for ^{14}C and CFC simultaneously. Then the circulation field of experiment B is presented, and the patterns of deep and bottom water flows as well as the transport rates of key water masses are described and discussed in the context of other published work. Table 1 shows that potential temperature misfits increase only marginally when ^{14}C and CFC are included and the potential temperature simulation is in very good agreement with the data in both cases.

a. Radiocarbon

Figure 3 shows the bottom water distribution of the natural radiocarbon for experiment B. In agreement with the data and consistent with the general concept of the global conveyor belt circulation (Broecker 1991), the model yields its highest $\Delta^{14}C$ values in the North Atlantic (−70‰ to −80‰) and lowest radiocarbon concentrations in the northeast Pacific (−235‰). The $\Delta^{14}C$ values in the Southern and Indian Oceans are intermediate and range between −150‰ and −165‰. There are clear signs of tongues with elevated $\Delta^{14}C$ values along the major deep and bottom water spreading paths. This includes the southward flow of North Atlantic Deep Water (NADW) in the North Atlantic and the northward spreading of Antarctic Bottom Water (AABW) in the western South Atlantic as well as in the South Pacific and the Indian Oceans. The quantitative agreement between simulated and measured $\Delta^{14}C$ values is excellent, and the model–data difference is only 1.3‰ on average (Table 1). The rms difference amounts to only 5.2‰ and is of the same order of magnitude as the uncertainties of the radiocarbon data. In the deep North Atlantic and parts of the Southern Ocean the measurements are systematically higher than the model simulations, owing to the contribution of bomb ^{14}C in these waters (Key et al. 2004; Rubin and Key 2002). Note that bomb radiocarbon is not included in the model, and contaminated data values are excluded and not assimilated in the model. The very good agreement between the model and the data also holds at other depth levels not shown here. At 2000-m depth, for instance, where the lowest $\Delta^{14}C$ values in the World Ocean are found in the northeast Pacific (−250‰), the

TABLE 1. Mean and rms potential temperature, radiocarbon, and CFC-11 model–data differences for runs without (experiment A) and with (experiment B) assimilation of ^{14}C and CFC data. Values in parentheses are deviations in percent of the respective mean observed concentrations.

	Expt A		Expt B	
	Mean	Rms	Mean	Rms
Bottom water θ (°C)				
Global	+0.030	0.05	+0.035	0.07
North Pacific	−0.005	0.04	+0.006	0.03
Bottom water $\Delta^{14}C$ (‰)				
Global	+47	21	+1.3	5.2
North Pacific	+66	23	+1.5	4.9
Bottom water CFC-11 (pmol kg^{-1}) (1998)				
Global	+0.32 (+120%)	0.57	−0.05	0.2
North Atlantic (equator–70°N)	+0.10 (+18%)	0.31	−0.06	0.25
South Pacific (40°S–equator)	+0.17 (+15 000%)	0.13	+0.003	0.01
South Atlantic (40°S–equator)	+0.07 (+110%)	0.17	+0.007	0.03
Indian Ocean (40°–10°S)	+0.11 (+600%)	0.13	−0.01	0.02
Southern Ocean (80°–40°S)	+0.81 (+190%)	0.75	−0.05	0.3
CFC-11 (pmol kg^{-1}) at 1700 m (1998)				
Global	0	0.5	−0.03	0.13
North Atlantic (equator–70°N)	−0.44 (−30%)	0.46	−0.05	0.25
South Pacific (40°S–equator)	+0.02 (+1000%)	0.04	−0.001	0.002
South Atlantic (40°S–equator)	+0.02 (+90%)	0.03	+0.005	0.01
Indian Ocean (40°–10°S)	+0.02 (+50%)	0.06	−0.02	0.05
Southern Ocean (80°–40°S)	+0.33 (+200%)	0.62	−0.03	0.1

mean and rms deviations are 0.3‰ and 5.6‰, respectively.

b. CFCs

The simulated CFC-11 bottom water concentrations for year 1998 are shown in Fig. 4 together with observations from the 1995–2000 period. As for radiocarbon, the simulated CFC-11 concentrations are in very good agreement with the data. High bottom water CFC-11 values are found in the northwest Atlantic and in the Southern Ocean at four locations around the Antarctic continent. In the North Atlantic the high-CFC bottom water concentrations are associated with deep-reaching convection in the Greenland, Norwegian, and Labrador Seas and the southward spreading of NADW in the DWBC. The highest bottom water CFC-11 concentrations in the Southern Ocean are found in the Weddell and Ross Seas as well as east of the Amery Basin and in the Australian–Antarctic Basin, indicating and confirming that deep convection and bottom water forma-

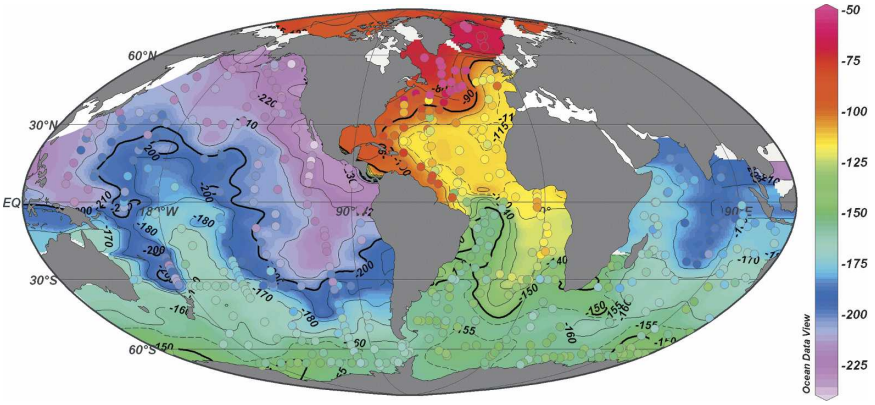

FIG. 3. Bottom water $\Delta^{14}C$ simulated by the model (color-shaded field) and from data (colored dots). Note that recently ventilated bottom waters in the North Atlantic and Southern Ocean are contaminated with bomb ^{14}C (Key et al. 2004). These samples are included in the plot, but they are not assimilated in the model. The mean model–data $\Delta^{14}C$ difference in areas not affected by bomb ^{14}C is +1.3 ‰, and the rms difference amounts to only 5.2‰.

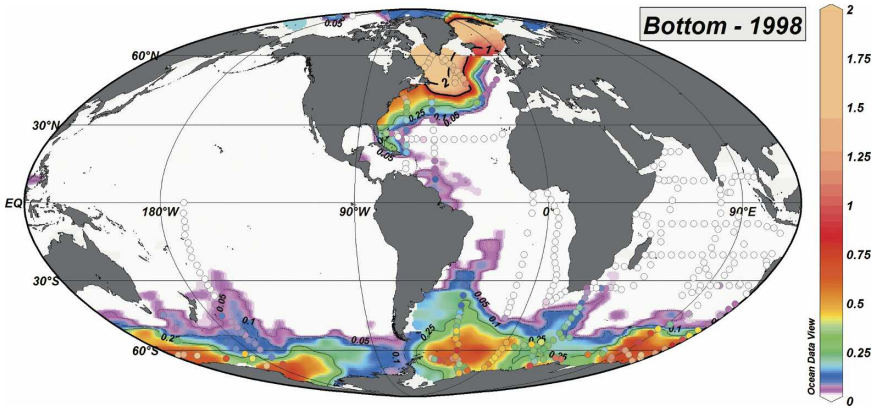

FIG. 4. Bottom water CFC-11 concentrations (pmol kg^{-1}) for year 1998 simulated by the model (color-shaded field) and data for the period 1995–2000 (colored dots). White color indicates very small CFC-11 concentrations below 0.025 pmol kg^{-1}. The mean model–data CFC-11 difference is -0.05 pmol kg^{-1}, and the rms difference amounts to only 0.2 pmol kg^{-1}.

tion are occurring at multiple sites around Antarctica and are not confined to the Weddell Sea (Orsi et al. 2002). Tongues of elevated CFC concentrations spread from polar areas equatorward and reveal major bottom water flows. This is most clearly seen in the Atlantic, where the southward-flowing NADW and northward-flowing AABW produce marked CFC patches that have almost reached the equator in 1998. Bottom water flows are also reflected in the CFC-11 distribution in the South Pacific near 170°W and in the south Indian Ocean (30°E and 80°–120°E). All the bottom water spreading paths evident in the CFC distribution coincide and are consistent with paths derived from the bottom water radiocarbon distribution in Fig. 3. The major difference between the two tracers is that because of their recent origin, CFC-11 has not penetrated entire basins yet, leaving most of the deep Pacific, Indian, and eastern Atlantic Ocean still essentially free of CFCs.

Figure 5 shows the simulated CFC-11 distribution at 1700-m depth for year 1998, together with available CFC-11 data for the period from 1995 to 2000. There is some similarity with the bottom water CFC-11 distribution in Fig. 4 with regard to the relatively high concentrations in polar and subpolar regions and the small values at low latitudes. However, at 1700-m depth there is a marked north–south asymmetry, with CFC concentrations in the North Atlantic being much larger than those in the Southern Ocean. The CFC signal in the North Atlantic associated with the southward flow of the upper NADW (uNADW) has progressed farther south compared to the bottom water and has reached the equator by 1998. There is evidence for southward uNADW transport across the equator and eastward transport along the equator. As for the bottom water, the agreement between the model simulation and data is very good globally (see Table 1).

The zonal sections at 26°N in the Atlantic (Fig. 6) show that the model is also able to reproduce details of the CFC-11 distribution within the DWBC. This includes location, vertical and zonal extent, as well as the amplitude of the double CFC-11 concentration maxima associated with the upper and lower NADW cores.

c. *Deep and bottom water circulation*

Figure 7 shows the meridional model flow velocities at 26°N in the North Atlantic for the same section as the CFC-11 distributions in Fig. 6. Clearly visible are two velocity maxima in the DWBC located near 1750- and 4200-m depth associated with the CFC-11 maxima at nearly the same locations. Within the DWBC cores, the long-term mean model flow velocities are on the order of 1 cm s^{-1}. It should be noted that the general patterns of the meridional velocity field are quite similar in the two solutions A and B and that the two separate upper and lower cores in the model DWBC at 26°N are already present in experiment A, which did not assimilate CFC data. This indicates that information on the detailed structure of the boundary current is contained in the temperature, salinity, oxygen, and nutrient data. The structure and strength of the DWBC calculated from the classical tracers alone (experiment A) are in surprisingly good agreement with the CFC data, as shown by the relatively small CFC-11 misfits of -30% and $+18\%$ in the upper and lower NADW branches of experiment A (Table 1). Only small adjustments to the velocity field in the North Atlantic are required in experiment B to achieve full consistency with the CFC observations. These adjustments result in small changes of watermass transports (see below), but

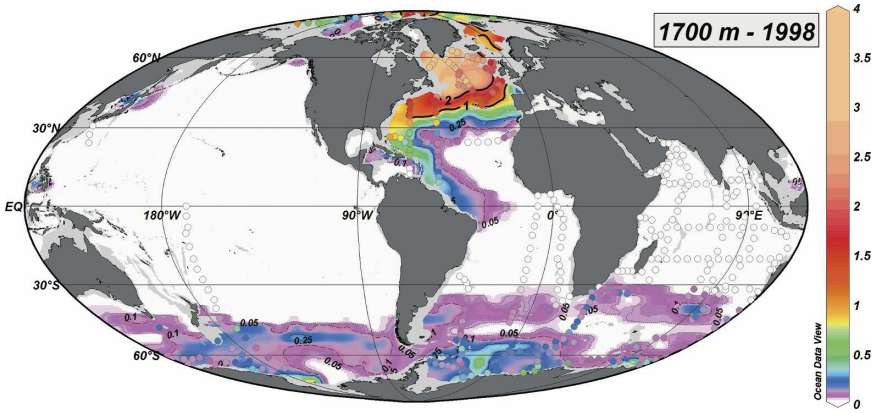

FIG. 5. As Fig. 4 but for 1700-m depth. The mean model–data CFC-11 difference is −0.03 pmol kg^{-1}, and the rms difference amounts to only 0.15 pmol kg^{-1}.

leave the flow patterns as shown in Fig. 7 largely unchanged.

Integrated water mass transports in the model are calculated for deep and bottom water layers using the interface definitions of Ganachaud and Wunsch (2000), which are based on the neutral density γ^n. The deep water layer ($27.72 < \gamma^n < 28.11$) is relatively thick and extends between circa 1200- and 4000-m depths in most of the low- and midlatitude ocean. In the Southern Ocean, this layer thins and rises to the surface, and south of 55°S it is typically located between 100- and 500-m depths. The entire water column below the deep water ($28.11 < \gamma^n$) represents the bottom water layer. Its thickness varies between a few hundred meters in

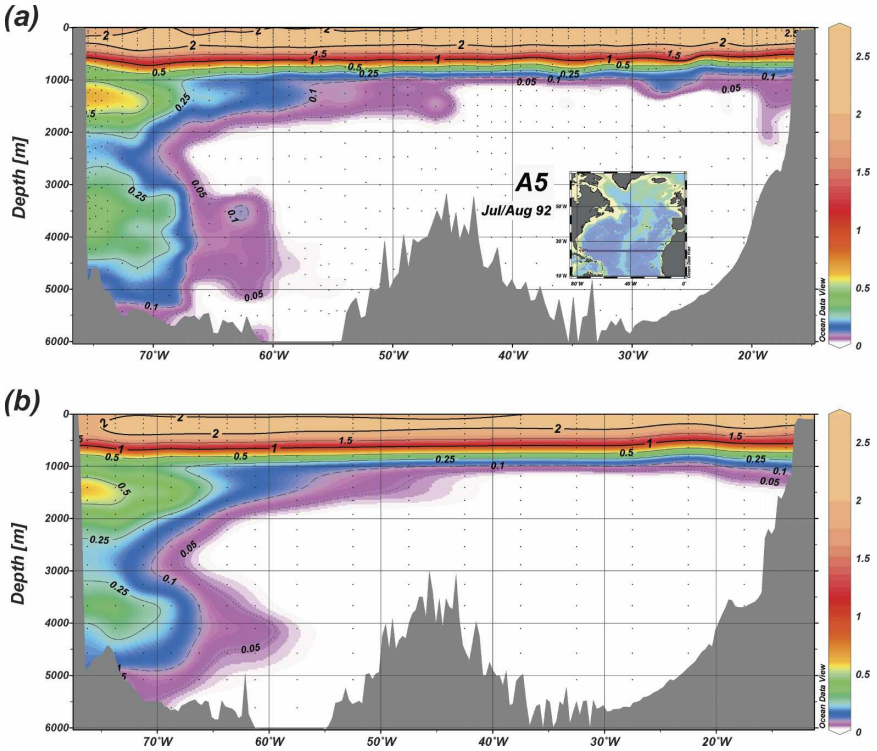

FIG. 6. CFC-11 concentrations (pmol kg^{-1}) along a zonal section at 24°N in the North Atlantic (a) from the WOCE A5 occupation in 1992 (Smethie et al. 2000) and (b) from the model simulations for 1992. Note that the model successfully reproduces the separate CFC-11 maxima of the upper and lower branches of the DWBC.

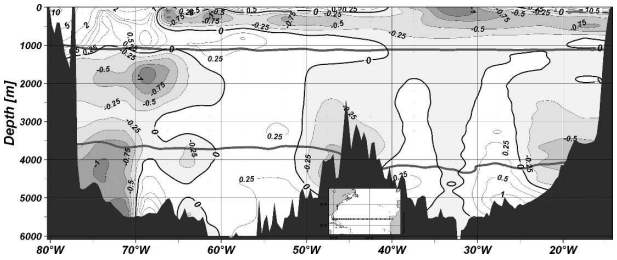

FIG. 7. Meridional model velocities at 26°N in the Atlantic for experiment B. Southward flows are gray shaded. Note the double velocity maxima for the upper and lower branches of the DWBC. The thick gray lines are neutral density isolines (γ^n = 27.72 and γ^n = 28.11) used as interfaces for layer transport calculations (Table 2 and Fig. 8).

the northeast Atlantic and North Pacific Oceans to almost the entire water column in the polar Southern Ocean. At mid- and low latitudes the mean thickness of the bottom water layer is about 1100 m. In the North Atlantic the deep water layer mainly represents the upper NADW (uNADW), while the lower NADW (lNADW) as well as the AABW are included in the bottom water layer (see Fig. 7 for γ^n isolines at 26°N). In the South Atlantic, the deep water layer encompasses uNADW and the largest part of lNADW, whereas the bottom water mainly represents the AABW. In the Southern Ocean the deep water density range corresponds to the upper Circumpolar Deep Water (CDW; Whitworth and Nowlin 1987), while the lower CDW and the AABW are part of the bottom water layer.

Schematic diagrams of the integrated deep and bottom water flows as well as transport estimates across selected cross sections and passages are shown in Fig. 8 for model experiment B. The deep water transport scheme (Fig. 8a) is dominated by the strong eastward flow of the deep ACC and a strong southward transport of the DWBC originating in the northern North Atlantic and continuing into the far South Atlantic. The transports of the DWBC in this layer are 14.7 Sv (Sv $\equiv 10^6\ m^3\ s^{-1}$) at 30°N and 8.6 Sv at 20°S. Near the equator a branch of the DWBC flows eastward and turns south along the African coast (2.2 Sv at 30°S). Another branch flows southeastward across the Brazil Basin, then turning eastward at about 20°S. In the model, there are three major counterclockwise recirculation gyres of the DWBC at 40°N, 20°N, and 40°S. The southern recirculation loop extends across the entire South Atlantic, while the recirculation at 40°N in the North Atlantic is confined to the western basin. In the Pacific and Indian Oceans the deep water flow pattern mainly consists of large, basin-scale gyres, and net meridional transports are apparently small.

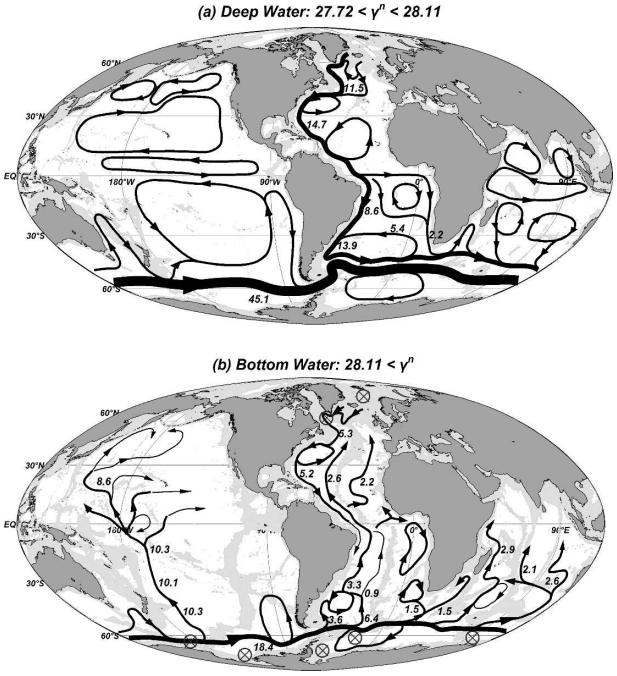

FIG. 8. Schematic circulation patterns and transports (Sv) of model flows for the (a) deep water and (b) bottom water layers. Regions with significant bottom water production in the North Atlantic and around Antarctica are marked.

The bottom water currents in Fig. 8b also exhibit a strong eastward flow associated with the ACC. Apart from this zonal component, the other main bottom water flows are mostly meridional, originating in polar regions and transporting bottom water equatorward. This includes the southward transport of lower NADW from the North Atlantic into the South Atlantic (5.2 Sv) and the northward transport of AABW from the Southern Ocean into the Pacific, Atlantic, and Indian Oceans. In the Pacific the dominant northward AABW transport is near 165°W. This flow passes through the Samoan Passage (10.3 Sv at 10°S) and continues into the northwestern Pacific. In the Atlantic the AABW flow is through the Vema and Hunter Channels (located at 28°S, 40°W and 33°S, 27°W, respectively; combined transport 4.2 Sv), passing through the Brazil Basin and continuing into the western North Atlantic (2.6 Sv at 20°N). The deep basins of the east Atlantic are renewed by bottom water flows through the Romanche and Vema Fracture Zones (equator–21°W, 11°N–42°W), and the Cape Basin is flushed by a clockwise flow of AABW (1.5 Sv). In the Indian Ocean there are three main branches of northward AABW flows: near 35°E into the Mozambique Basin; near 55°E via the Crozet Basin into the Madagascar, Mascarene, and Somali Basins; and near 90°E into the South Australian,

TABLE 2. Zonally integrated volume transports (Sv) for the deep and bottom water layers. The transport values are for experiment B, which produces realistic ^{14}C and CFC distributions. Values in parentheses are for experiment A, showing large and systematic ^{14}C and CFC misfits.

Ocean	$27.72 < \gamma^n < 28.11$	$28.11 < \gamma^n$
Atlantic		
50°N	−11.5 (−13.1)	−4.2 (−2.8)
30°N	−14.7 (−15.8)	−3.2 (−2.6)
30°S	−15.6 (−16.1)	+1.5 (+1.8)
Indian		
30°S	−4.0 (−19.8)	+5.5 (+17.2)
Pacific		
30°N	−3.2 (−6.3)	+5.3 (+9.8)
30°S	−6.4 (−12.5)	+9.8 (+19.3)
Southern		
50°S	−28.0 (−58.7)	+17.9 (+36.5)
58°S	−25.5 (−58.4)	+14.1 (+46.9)

West Australian, and Central Indian Basins. Each of these bottom water flows carries between 2 and 3 Sv of AABW northward.

Zonally integrated layer transports for the deep and bottom water layers are listed in Table 2. In the Atlantic, experiment B shows combined southward NADW transports of 15.7, 17.9, and 15.6 Sv at 50°N, 30°N, and 30°S, and a relatively small net northward transport in the bottom layer at 30°S (1.5 Sv). The small net bottom layer transport arises because some of the southward transport of lNADW occurs in the bottom layer, which partially compensates for the northward AABW flux. There are only small differences among the zonally integrated transports in the Atlantic between experiments A and B. As noted above, A already achieves reasonable agreement with the CFC data in the North Atlantic (see Table 1), and only minor modifications are obviously required for full consistency.

CFC concentrations in South Atlantic bottom waters are highly sensitive to even small changes in the strength of the bottom water flows, as indicated by experiment A, which has only slightly higher (relative to experiment B) AABW transports through the Vema and Hunter Channels (5.2 Sv as compared with 4.2 Sv for B) and a slightly higher net bottom layer transport at 30°S (1.8 Sv as compared with 1.5 Sv for B). Yet these small transport differences are sufficient to produce CFC concentrations in the deep and bottom waters that exceed the observations by about 100% (Table 1). These significant CFC misfits in the South Atlantic are corrected in experiment B by a reduction of the northward AABW transport of about 1 Sv.

Both the Pacific and Indian Oceans show a meridional overturning consisting of northward bottom water flows and southward return flows in the deep water layer. In the Pacific, the net northward bottom water transports are 9.8 Sv at 30°S and 5.3 Sv at 30°N. The deep water return flows at these latitudes are somewhat smaller and amount to −6.4 and −3.2 Sv, respectively. At 30°S in the Indian Ocean, the net northward bottom water transport is 5.5 Sv, and the deep water return flow amounts to −4 Sv. There are drastic transport reductions between experiments A and B for all the integrated abyssal flows in the Pacific and Indian Oceans (Table 2). While the large northward AABW transports into the Pacific (19.3 Sv) and Indian Oceans (17.2 Sv) in experiment A are found to be compatible with the set of traditional tracers (*T*, *S*, oxygen, nutrients), they result in very large overestimations of the radiocarbon and CFC concentrations in the deep and bottom waters (Table 1) and produce CFC tongues that extend much too far into the Pacific and Indian Oceans. To reach consistency with the ^{14}C and CFC data, bottom water transports into the Indian and Pacific Oceans have to be reduced in experiment B by factors of 3 and 2, respectively.

Corresponding to the large differences in bottom water transports in the Pacific and Indian Oceans, there are also large differences in the production and export of dense bottom water from the Southern Ocean. Experiment A exhibits very vigorous vertical overturning in the Southern Ocean and a net equatorward AABW export of about 40 Sv at 55°S (Table 2). This large bottom water export feeds the large AABW inflows into the Pacific and Indian Oceans described above and is responsible for the much too high radiocarbon and CFC deep and bottom water values over the entire Southern Ocean (Table 1). Again, radiocarbon and CFC data are seen to provide additional constraints on water mass formation and transport rates not provided by the classical hydrographic parameters. This holds especially in the Southern Ocean. To achieve consistency with these tracers a threefold reduction of the export rate of AABW at 55°S to about 16 Sv is required in experiment B (Table 2). The 16 Sv of newly formed dense bottom water from the Southern Ocean are of comparable size as the contribution of NADW from the North Atlantic.

The general patterns of deep and bottom water flows and most of the transport estimates in Fig. 8 and Table 2 are consistent with published work based either on direct observations or model reconstructions. In the subpolar North Atlantic there is broad agreement with the deep water circulation derived from current-meter observations and hydrographic sections (Schott et al. 2004), with the middepth circulation obtained from neutrally buoyant floats (Lavender et al. 2005), and with the spreading pathways of Labrador Sea Water

(LSW) obtained from inverse model analysis of hydrographic lines (Paillet et al. 1998). In addition, the combined deep and bottom water transport of 16.8 Sv in the DWBC at the latitude of the Grand Banks agrees very well with the 16-Sv estimate of Schmitz and McCartney (1993) and the 17.2-Sv NADW formation rate of Smethie and Fine (2001). The mean spreading rate of circa 1 cm s^{-1} in the model's DWBC at 26°N is consistent with independent estimates based on CFC data (Smethie et al. 2000; Smethie 1993; Weiss et al. 1985). These studies also find evidence for strong recirculation gyres and exchanges of the DWBC with the basin interior, consideration of which helps to reconcile the apparent mismatch between current-meter velocity measurements and tracer-based spreading rates.

The deep and bottom water flows in the tropical Atlantic are consistent with the scheme of McCartney (1993) and the zonal deep water flows in the Brazil Basin are in agreement with the analysis of Treguier et al. (2003) using float data and dynamical model results. The deep water flow directions of the model in the South Atlantic are also consistent with the ^{3}He distributions of Rüth et al. (2000), which indicate westerly flow over the Mid-Atlantic Ridge at 30°S, and little net zonal flows at 19° and 11°S. In the Argentine Basin the bottom water circulation resembles the patterns found by Peterson (1992) and Coles et al. (1996).

The northward model transport of 3.3 Sv of AABW through the Vema Channel is somewhat smaller than the direct current measurements and dynamic calculations of Hogg et al. (1982) and McDonagh et al. (2002) (4 ± 1.2 and 3.7 Sv, respectively). A major discrepancy is found in the Hunter Channel, where the model flow (0.9 Sv) is small relative to the transport estimate of 2.9 ± 1.2 Sv by Zenk et al. (1999). The combined northward AABW model transport of 4.2 Sv is significantly smaller than the 6.9 ± 1.2 Sv estimate of Hogg (2001). Given the large sensitivity of bottom water CFC concentrations in the southwest Atlantic to even slight increases of the northward bottom water transport (as indicated by experiment A; see above), an AABW transport of 6.9 Sv appears to be incompatible with CFC data and the model transport of 4.2 Sv is considered to be an upper limit for the long-term mean northward AABW transport across 30°S in the Atlantic. Consistent with the present study, Meredith et al. (2001) also report rather small northward AABW transports on the basis of a CFC data analysis in the Southern Ocean and South Atlantic, and McDonagh et al. (2002) using hydrographic sections find an even smaller net AABW flow of 1.7 ± 1.1 Sv through the Vema Channel.

In the Pacific and Indian Oceans the bottom water circulation pattern (Fig. 8b) is consistent with previous work (Fukasawa et al. 2004; Hogg 2001; Kawabe et al. 2003; Mantyla and Reid 1995; van Aken et al. 2004; Warren and Johnson 2002), and the deep water flow directions in the central and eastern Pacific as well as in the Indian Ocean (Fig. 8a) agree with the spreading directions of deep water ^{3}He plumes originating from hydrothermal vents (Lupton 1998; Srinivasan et al. 2004). The northward model transport of AABW through the Samoan Passage (10.3 Sv) is virtually identical with the estimate of Roemmich et al. (1996) (10.6 ± 1.6 Sv) based on current-meter measurements combined with hydrographic sections.

The zonally integrated layer transports in Table 2 agree with the results of Ganachaud and Wunsch (2000) and Ganachaud et al. (2000) within their error bars. There are only two exceptions: the net 6 ± 1.6 Sv northward bottom water transport in the South Atlantic found by Ganachaud and Wunsch (2000) appears to be too large and incompatible with the CFC data (see discussion above) and the bottom water transport across 25°N in the North Pacific (1.5 ± 1 Sv) appears to be small relative to the 5.3 Sv in experiment B. It remains to be verified whether such small bottom water inflows are compatible with the radiocarbon balance of the deep North Pacific.

The net northward transport below 3200 m into the Indian Ocean of 17 Sv shown by Ferron and Marotzke (2003) is much larger than the 5.5 Sv in experiment B for the same cross section and appears to be inconsistent with the CFC observations. Experiment A, with about the same net northward transport into the Indian Ocean as in Ferron and Marotzke (2003), produces bottom water CFC-11 concentrations that are on average 0.11 pmol kg^{-1} or 600% higher than the observations.

The finding in the present model that the production rates of deep and bottom waters in the North Atlantic and Southern Oceans are of about the same magnitude (about 16 Sv) is consistent with the study of Orsi et al. (2002), who exploited CFC inventories in the Southern Ocean for the estimation of watermass production rates, and is also in agreement with the postulations of Broecker et al. (1998) on the basis of the PO_4^* parameter. Many previous AABW production estimates (see Fahrbach et al. 2001; Foldvik et al. 2004 and references therein) are much smaller; however, values are often difficult to compare because of differences in the watermass definitions used and because most studies focus on specific regions and do not provide circum-Antarctic production rates. Garabato et al. (2002) find significant AABW production in the Weddell Sea and a northward transport into the Scotia Sea of 9.7 ± 3.7 Sv. This rate is compatible with the present study and the result

of Orsi et al. (2002), when combined with contributions from other production sites in the Southern Ocean. In the model, there are four regions around the Antarctic continent where significant downwelling of dense and CFC-rich waters occurs: the Weddell and Ross Seas, the region east of the Amery Basin, and the Australian–Antarctic Basin (Fig. 8b). All of these areas show enhanced CFC concentrations at the bottom.

d. CFC forecast

It has been shown above that model solution B produces radiocarbon and CFC distributions that are in very good agreement with the available observations. Here, this solution is combined with best-guess estimates of atmospheric CFC trends for the next 70 yr (WMO 2003) to simulate the evolution of oceanic CFC distributions in the foreseeable future. This experiment implicitly assumes that the ocean circulation remains unchanged with time and that temporal CFC changes in the ocean are driven by atmospheric CFC changes only. The results of this run allow for the identification of the regions of largest future CFC changes in the ocean, provide guidance for future CFC observational programs, and can serve as benchmark distributions against which future CFC observations can be compared. Major differences between predictions and future data may be indications of changes in the ocean circulation.

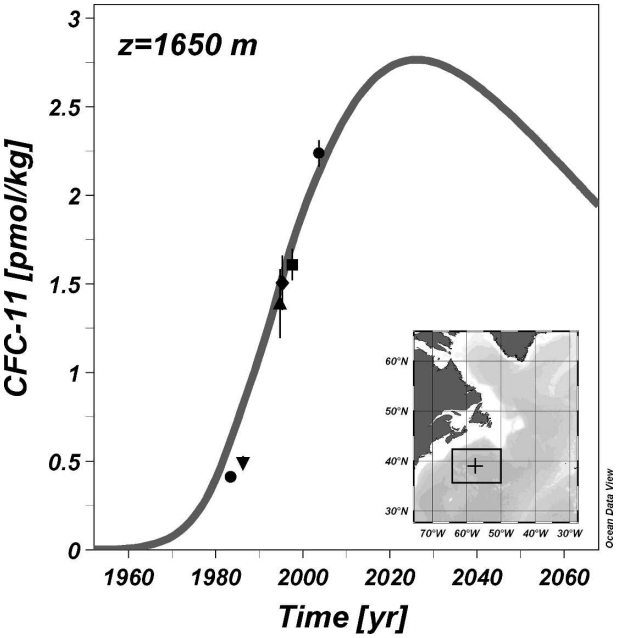

FIG. 9. Temporal evolution of CFC-11 concentrations in the upper NADW as simulated by the model (thick gray line) and from observations (black symbols). The data points are averages of observations between 1550- and 1750-m depth of available stations from the box marked in the map, and the error bars indicate mean standard errors. The model curve is for the location marked with a cross (+).

According to the WMO (2003) prediction, the atmospheric concentrations of CFC-11 and CFC-12 will decrease over the next 70 yr. Because of differences in the emissions and lifetimes of the two substances, however, the timing and amplitude of the decreases are different. CFC-11 concentrations reached their maximum in the mid-1990s and have been decreasing since then. The future decrease is expected to be nearly exponential with a lifetime of 45 yr. By 2030 the anticipated atmospheric CFC-11 concentrations are expected to be only 60% of their present values. For CFC-12, the decrease has only begun in recent years, and its rate of change will be slower because of continued emissions and a larger estimated atmospheric lifetime (100 yr). In 2030 the predicted atmospheric CFC-12 concentrations will be about 80% of their present levels.

Figure 9 shows the model-simulated temporal evolution of the CFC-11 concentrations in the upper branch of the DWBC at 40°N in the North Atlantic together with available measurements from the region. The data and simulation are in very good agreement and show rapid concentration increases during the period from 1980 to 2010. Afterward, the rate of increase declines, and maximal CFC-11 concentrations in the uNADW at this location are expected for 2025. At locations farther south in the DWBC the general trends are similar to those in Fig. 9, but the concentration maxima appear later in time and the subsequent decreases are slower. In the tropical Atlantic, CFC-11 concentrations in uNADW and lNADW will continue to increase beyond 2060.

The temporal evolution of CFC-11 in the bottom waters of the global ocean are shown in Fig. 10. It is found that of all ocean basins the western Atlantic is the one that is most rapidly flushed with CFC-bearing bottom waters, and that this invasion is occurring at comparable rates from the north and south. By 2030 the bottom water CFC-11 concentrations in the entire western Atlantic are expected to exceed 0.1 pmol kg^{-1}. CFC-rich bottom waters also spread into the South Pacific and into the Indian Ocean along the bottom water pathways depicted in Fig. 8b; however, the spatial extent is limited, and by 2030 the bottom water CFC-11 concentrations in most of the Indian Ocean and North Pacific are expected to remain below 0.1 pmol kg^{-1}. CFC-11 bottom concentrations above the current detection limit of 0.02 pmol kg^{-1} are expected for 2030 in the entire Atlantic, up to about 20°S in the Indian Ocean and as far north as 15°N in the central Pacific (180°). According to the present model, bottom water

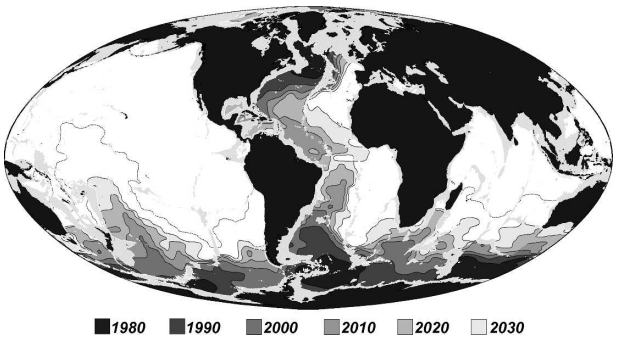

FIG. 10. Temporal evolution of areas with bottom water CFC-11 concentrations greater than 0.1 pmol kg^{-1}. Note that by 2030 the entire deep western Atlantic exceeds the prescribed limit, while predicted bottom water CFC concentrations in most of the eastern Atlantic as well as in the Indian and Pacific Oceans remain very small. The dotted line represents the 0.02 pmol kg^{-1} contour in 2030.

CFC-11 concentrations in 2030 will remain below the detection limit in the entire northeast Pacific and in the Indian Ocean north of 10°S.

4. Summary and conclusions

The adjoint method has been applied successfully for the assimilation of natural radiocarbon and chlorofluorocarbon (CFC) data in a coarse-resolution global ocean model with steady circulation. This is an extension of previous work, for which only the classical hydrographic parameters temperature, salinity, oxygen, nutrients, dissolved inorganic carbon, and alkalinity were used. Model experiment B shows that realistic global ocean distributions of hydrographic parameters and tracers can be obtained simultaneously. The radiocarbon simulations correctly reproduce the observed ^{14}C decrease along the global conveyor belt circulation, and the modeled concentrations differences between the deep western North Atlantic and North Pacific are in excellent agreement with the data. The model also correctly reproduces the positions and the spatial extent of the tongues of enhanced ^{14}C that spread southward along the path of the DWBC in the Atlantic and along the northward transport routes of AABW from the Southern Ocean into the Pacific and Indian Oceans. The oceanic distributions of the CFCs as well as their temporal evolution are also represented realistically in the model. This includes a very good agreement of deep and bottom water CFC concentrations in watermass formation areas and the correct simulation of the spatial extent as well as the temporal progression of CFC plumes along the abyssal flow paths. The model also captures details of the deep CFC transports, such as the double concentration maxima in the upper and lower branches of the DWBC in the Atlantic. Overall, the mean model–data differences for ^{14}C and CFCs are very small and the rms differences are only slightly higher than the data errors.

The patterns of deep and bottom water flows that reproduce the observed ^{14}C and CFCs fields are consistent with previous results based on direct flow measurement, analysis of hydrographic and tracer observations, and a large variety of model studies. The transport estimates for deep and bottom water flows in the present model in many cases confirm published values. This holds, for instance, for the southward transport of the DWBC in the Atlantic and for the northward transport of AABW through the Samoan Passage in the South Atlantic.

The analysis of results from experiment A, which is not fitted to radiocarbon and CFC data, and which exhibits large northward AABW bottom water flows into all three oceans (Pacific, Atlantic, and Indian), reveals a large sensitivity of CFC and ^{14}C concentrations to changes in the strengths of the bottom currents. In experiment A the large bottom water transports lead to large overestimations of deep and bottom water CFC and ^{14}C values, and these transports turn out to be incompatible with the tracer data. CFC and ^{14}C provide independent information not included in the classical hydrographic parameters, which allows us to place upper bounds on the deep and bottom water transports, especially in the Southern Ocean.

In the Southern Ocean the model shows that a long-term mean AABW transport through the Vema and Hunter Channels of 4.2 Sv is in agreement with the tracer data, while transports of more than 5 Sv are incompatible with CFC data in this region. Similarly, in the Indian Ocean the net northward transport of bottom water ($\gamma^n > 28.11$) across 30°S consistent with CFC and ^{14}C data is 5.5 Sv, while transport values above 10 Sv are seen to be incompatible with CFC observations.

In the Southern Ocean the bottom water CFC and ^{14}C concentrations are very sensitive to the strength of the vertical overturning and to the production rate of AABW. Comparison with results from experiment A, which exhibits a large AABW production rate and very large CFC and ^{14}C misfits, allows narrowing the range for the production and export of AABW from the Southern Ocean. The net circum-Antarctic northward AABW ($\gamma^n > 28.11$) flux at 55°S in experiment B is 16 Sv. The misfits in experiment A indicate that AABW transports larger than 20 Sv are incompatible with the CFC data.

CFC forecast calculations show that the deep western Atlantic is rapidly flushed with CFC-bearing waters,

and by 2030, CFC-11 concentrations are expected to be higher than 0.1 pmol kg^{-1} everywhere in the deep western Atlantic. The large temporal CFC concentration increases presently observed in deep and bottom water masses will slow down in the Atlantic, and deep water CFC-11 concentrations near the production areas will actually start to decrease in 5–10 yr. CFC will also penetrate into the Pacific and Indian Oceans; however, by 2030 the bottom water CFC-11 concentrations will remain below the detection limit in the entire northeast Pacific and in the Indian Ocean north of 10°S.

Acknowledgments. Concepts for the use and assimilation of tracer data in inverse models were discussed and developed together with Carl Wunsch during a two-year stay at MIT. I thank him for uncounted hours of interesting and inspiring discussions and for his continued support over the years. This study would not have been possible without the efforts of those responsible for collecting and analyzing CFCs and ^{14}C and making those measurements available. They include C. Andrie, J. Bullister, R. Fine, P. Jones, R. M. Key, L. Memery, M. Rhein, P. Quay, W. Roether, W. Smethie, D. Smythe-Wright, M. Warner, Y. Watanabe, A. Watson, R. Weiss, and C. S. Wong.

REFERENCES

Andrie, C., M. Rhein, S. Freudenthal, and O. Plaehn, 2002: CFC time series in the deep water masses of the western tropical Atlantic, 1990-1999. *Deep-Sea Res. I,* **49,** 281–304.

Böning, C. W., M. Rhein, J. Dengg, and C. Dorow, 2003: Modeling CFC inventories and formation rates of Labrador Sea Water. *Geophys. Res. Lett.,* **30,** 1050, doi:10.1029/2002GL014855.

Broecker, W. S., 1991: The great ocean conveyor. *Oceanography,* **4,** 79–89.

——, and T.-S. Peng, 1982: *Tracers in the Sea*. Lamont-Doherty Geological Observatory, 690 pp.

——, and Coauthors, 1998: How much deep water is formed in the Southern Ocean? *J. Geophys. Res.,* **103,** 15 833–15 843.

Bullister, J. L., and R. F. Weiss, 1983: Anthropogenic chlorofluoromethanes in the Greenland and Norwegian Seas. *Science,* **221,** 265–268.

Coles, V. J., M. S. McCartney, D. B. Olson, and W. M. Smethie, 1996: Changes in Antarctic Bottom Water properties in the western South Atlantic in the late 1980s. *J. Geophys. Res.,* **101,** 8957–8970.

de las Heras, M., and R. Schlitzer, 1999: On the importance of intermediate water flows for the global ocean overturning. *J. Geophys. Res.,* **104,** 15 515–15 536.

Dutay, J.-C., and Coauthors, 2002: Evaluation of ocean model ventilation with CFC-11: comparison of 13 global ocean models. *Ocean Modell.,* **4,** 89–102.

England, M. H., and E. Maier-Reimer, 2001: Using chemical tracers to assess ocean models. *Rev. Geophys.,* **39,** 29–70.

Fahrbach, E., S. Harms, G. Rohardt, M. Schröder, and R. A. Woodgate, 2001: Flow of bottom water in the northwestern Weddell Sea. *J. Geophys. Res.,* **106,** 2761–2778.

Feely, R. A., C. L. Sabine, R. Schlitzer, J. L. Bullister, S. Mecking, and D. Greeley, 2004: Oxygen utilization and organic carbon remineralization in the Pacific Ocean. *J. Oceanogr.,* **60,** 45–52.

Ferron, B., and J. Marotzke, 2003: Impact of 4D-variational assimilation of WOCE hydrography on the meridional circulation of the Indian Ocean. *Deep-Sea Res. II,* **50,** 2005–2021.

Fiadeiro, M. E., 1982: Three-dimensional modeling of tracers in the deep Pacific Ocean: II. Radiocarbon and the circulation. *J. Mar. Res.,* **40,** 537–550.

Fine, R. A., M. Rhein, and C. Andrie, 2002: Using a CFC effective age to estimate propagation and storage of climate anomalies in the deep western North Atlantic Ocean. *Geophys. Res. Lett.,* **29,** 2227, doi:10.1029/2002GL015618.

Foldvik, A., and Coauthors, 2004: Ice shelf water overflow and bottom water formation in the southern Weddell Sea. *J. Geophys. Res.,* **109,** C02015, doi:10.1029/2003JC002008.

Fukasawa, M., H. Freeland, R. Perkin, T. Watanabe, H. Uchida, and A. Nishina, 2004: Bottom water warming in the North Pacific Ocean. *Nature,* **428,** 825–827.

Ganachaud, A., and C. Wunsch, 2000: Improved estimates of global ocean circulation, heat transport and mixing from hydrographic data. *Nature,* **408,** 453–457.

——, ——, J. Marotzke, and J. Toole, 2000: Meridional overturning and large-scale circulation of the Indian Ocean. *J. Geophys. Res.,* **105,** 26 117–26 134.

Garabato, A. C. N., E. L. McDonagh, D. P. Stevens, K. J. Heywood, and R. J. Sanders, 2002: On the export of Antarctic Bottom Water from the Weddell Sea. *Deep-Sea Res. II,* **49,** 4715–4742.

Harwell, 1995: *Harwell Subroutine Library.* Release 12, Vol. 1, 681 pp.

Hestenes, M. R., 1975: *Optimization Theory*. John Wiley and Sons, 447 pp.

Hogg, N. G., 2001: Quantification of the deep circulation. *Ocean Circulation and Climate: Observing and Modelling the Global Ocean,* G. Siedler, J. Church, and J. Gould, Eds., Academic Press, 259–270.

——, P. Biscaye, W. Gardner, and W. J. Schmitz Jr., 1982: On the transport and modification of Antarctic Bottom Water in the Vema Channel. *J. Mar. Res.,* **40** (Suppl.), 231–263.

Kawabe, M., S. Fujio, and D. Yanagimoto, 2003: Deep-water circulation at low latitudes in the western North Pacific. *Deep-Sea Res. I,* **50,** 631–656.

Key, R. M., and Coauthors, 2004: A global ocean carbon climatology: Results from Global Data Analysis Project (GLODAP). *Global Biogeochem. Cycles,* **18,** GB4031, doi:10.1029/2004GB002247.

Lavender, K. L., W. B. Owens, and R. E. Davis, 2005: The mid-depth circulation of the subpolar North Atlantic Ocean as measured by subsurface floats. *Deep-Sea Res. I,* **52,** 767–785.

Le Dimet, F.-X., and O. Talagrand, 1986: Variational algorithms for analysis and assimilation of meteorological observations: Theoretical aspects. *Tellus,* **38,** 97–110.

Lupton, J., 1998: Hydrothermal helium plumes in the Pacific Ocean. *J. Geophys. Res.,* **103,** 15 853–15 868.

Mantyla, A. W., and J. L. Reid, 1995: On the origins of deep and bottom waters of the Indian Ocean. *J. Geophys. Res.,* **100,** 2417–2439.

Marshall, J., and F. Schott, 1999: Open-ocean convection: Observations, theory, and models. *Rev. Geophys. Space Phys.,* **37,** 1–64.

Matear, R. J., C. S. Wong, and L. Xie, 2003: Can CFCs be used to

determine anthropogenic CO2? *Global Biogeochem. Cycles,* **17,** 1013, doi:10.1029/2001GB001415.

Matsumoto, K., and Coauthors, 2004: Evaluation of ocean carbon cycle models with data-based metrics. *Geophys. Res. Lett.,* **31,** L07303, doi:10.1029/2003GL018970.

McCartney, M. S., 1993: Crossing of the equator by the deep western boundary current in the western Atlantic Ocean. *J. Phys. Oceanogr.,* **23,** 1953–1974.

McDonagh, E. L., M. Arhan, and K. J. Heywood, 2002: On the circulation of bottom water in the region of the Vema Channel. *Deep-Sea Res. I,* **49,** 1119–1139.

Meredith, M. P., A. J. Watson, K. A. Van Scoy, and T. W. N. Haine, 2001: Chlorofluorocarbon-derived formation rates of the deep and bottom waters of the Weddell Sea. *J. Geophys. Res.,* **106,** 2899–2919.

Orr, J. C., and Coauthors, 2001: Ocean CO_2 sequestration efficiency from 3-D ocean model comparison. *Greenhouse Gas Control Technologies,* D. Williams et al., Eds., Elsevier Science, 469–474.

Orsi, A. H., W. M. Smethie, and J. L. Bullister, 2002: On the total input of Antarctic waters to the deep ocean: A preliminary estimate from chlorofluorocarbon measurements. *J. Geophys. Res.,* **107,** 3122, doi:10.1029/2001JC000976.

Paillet, J., M. Arhan, and M. S. McCartney, 1998: Spreading of Labrador Sea Water in the eastern North Atlantic. *J. Geophys. Res.,* **103,** 10 223–10 239.

Peterson, R. G., 1992: The boundary currents in the western Argentine Basin. *Deep-Sea Res.,* **39A,** 623–644.

Reid, J. L., 1997: On the total geostrophic circulation of the Pacific Ocean: flow patterns, tracers, and transports. *Progress in Oceanography,* Vol. 39, Pergamon, 263–352.

Rhein, M., and Coauthors, 2002: Labrador Sea Water: Pathways, CFC inventory, and formation rates. *J. Phys. Oceanogr.,* **32,** 648–665.

Roemmich, D., S. Hautala, and D. Rudnick, 1996: Northward abyssal transport through the Samoan Passage and adjacent regions. *J. Geophys. Res.,* **101,** 14 039–14 055.

Rubin, S. I., and R. M. Key, 2002: Separating natural and bomb-produced radiocarbon in the ocean: The potential alkalinity method. *Global Biogeochem. Cycles,* **16,** 1105, doi:10.1029/2001GB001432.

Rüth, C., R. Well, and W. Roether, 2000: Primordial ^{3}He in South Atlantic deep waters from sources on the Mid-Atlantic Ridge. *Deep-Sea Res. I,* **47,** 1059–1075.

Schlitzer, R., 1993: Determining the mean, large-scale circulation of the Atlantic with the adjoint method. *J. Phys. Oceanogr.,* **23,** 1935–1952.

——, 1995: An adjoint model for the determination of the mean oceanic circulation, air-sea fluxes and mixing coefficients. Ber. zur Polarforschung 156, Alfred Wegener Institute, 103 pp.

——, 2000: Applying the adjoint method for global biogeochemical modeling. *Inverse Methods in Global Biogeochemical Cycles, Geophys. Monogr.,* Vol. 114, Amer. Geophys. Union, 107–124.

——, 2002: Carbon export fluxes in the Southern Ocean: Results from inverse modeling and comparison with satellite based estimates. *Deep-Sea Res. II,* **49,** 1623–1644.

——, 2004: Export production in the equatorial and North Pacific derived from dissolved oxygen, nutrient and carbon data. *J. Oceanogr.,* **60,** 53–62.

——, R. Usbeck, and G. Fischer, 2004: Inverse modeling of particulate organic carbon fluxes in the South Atlantic. *The South Atlantic in the Late Quaternary—Reconstruction of Material Budget and Current Systems,* G. Wefer, S. Mulitza, and V. Rathmeyer, Eds., Springer, 1–19.

Schmitz, W. J., Jr., and M. S. McCartney, 1993: On the North Atlantic circulation. *Rev. Geophys.,* **31,** 29–49.

Schott, F. A., R. Zantopp, L. Stramma, M. Dengler, J. Fischer, and M. Wibaux, 2004: Circulation and deep-water export at the western exit of the subpolar North Atlantic. *J. Phys. Oceanogr.,* **34,** 817–843.

Smethie, W. M., Jr., 1993: Tracing the thermohaline circulation in the western north Atlantic using chlorofluorocarbons. *Progress in Oceanography,* Vol. 31, Pergamon, 51–99.

——, and R. A. Fine, 2001: Rates of North Atlantic Deep Water formation calculated from chlorofluorocarbon inventories. *Deep-Sea Res. I,* **48,** 189–215.

——, and S. S. Jacobs, 2005: Circulation and melting under the Ross Ice Shelf: Estimates from evolving CFC, salinity and temperature fields in the Ross Sea. *Deep-Sea Res. I,* **52,** 959–978.

——, R. A. Fine, A. Putzka, and E. P. Jones, 2000: Tracing the flow of North Atlantic Deep Water using chlorofluorocarbons. *J. Geophys. Res.,* **105,** 14 297–14 323.

Srinivasan, A., Z. Top, P. Schlosser, R. Hohmann, M. Iskandarani, D. B. Olson, J. E. Lupton, and W. J. Jenkins, 2004: Mantle ^{3}He distribution and deep circulation in the Indian Ocean. *J. Geophys. Res.,* **109,** C06012, doi:10.1029/2003JC002028.

Thacker, W. C., and R. B. Long, 1988: Fitting dynamics to data. *J. Geophys. Res.,* **93,** 1227–1240.

Treguier, A. M., N. G. Hogg, M. Maltrud, K. Speer, and V. Thierry, 2003: The origin of deep zonal flows in the Brazil Basin. *J. Phys. Oceanogr.,* **33,** 580–599.

van Aken, H. M., H. Ridderinkhof, and W. P. M. de Ruijter, 2004: North Atlantic deep water in the south-western Indian Ocean. *Deep-Sea Res. I,* **51,** 755–776.

Walker, S. J., R. F. Weiss, and P. K. Salameh, 2000: Reconstructed histories of the annual mean atmospheric mole fractions for the halocarbons CFC-11, CFC-12, CFC-113 and carbon tetrachloride. *J. Geophys. Res.,* **105,** 14 285–14 296.

Warren, B. A., and G. C. Johnson, 2002: The overflows across the Ninetyeast Ridge. *Deep-Sea Res. II,* **49,** 1423–1439.

Weiss, R. F., J. L. Bullister, R. H. Gammon, and M. J. Warner, 1985: Atmospheric chlorofluoromethanes in the deep equatorial Atlantic. *Nature,* **314,** 608–610.

Whitworth, T., III, and W. D. Nowlin Jr., 1987: Water masses and currents of the Southern Ocean at the Greenwich meridian. *J. Geophys. Res.,* **92,** 6462–6476.

WMO, 2003: *WMO (World Meteorological Organization) Scientific Assessment of Ozone Depletion: 2002.* Global Ozone Research and Monitoring Project 47, WMO, 498 pp.

WOCE Data Products Committee, 2002: WOCE global data, version 3.0. WOCE International Project Office Rep. 180102, DVD-ROM.

Wunsch, C., and B. Grant, 1982: Towards the general circulation of the north Atlantic Ocean. *Progress in Oceanography,* Vol. 11, Pergamon, 1–59.

——, D.-X. Hu, and B. Grant, 1983: Mass, heat, salt and nutrient fluxes in the South Pacific Ocean. *J. Phys. Oceanogr.,* **13,** 725–753.

Zenk, W., G. Siedler, and B. Lenz, 1999: Antarctic bottom water flow through the Hunter Channel. *J. Phys. Oceanogr.,* **29,** 2785–2801.